Earth and Planetary Science Letters 309 (2011) 198–206

Contents lists available at ScienceDirect

Earth and Planetary Science Letters

journal homepage: www.elsevier.com/locate/epsl

A chondrule-like object captured by space-exposed aerogel on the international space station

T. Noguchi [a,*], T. Nakamura [b], T. Ushikubo [c], N.T. Kita [c], J.W. Valley [c], R. Yamanaka [d], Y. Kimoto [d], Y. Kitazawa [e,d]

[a] College of Science, Ibaraki University, 2-1-1 Bunkyo, Mito, Ibaraki 310-8512, Japan
[b] Department of Earth Science, Graduate School of Science, Tohoku University, 6-3 Aramaki Aza-Aoba, Aoba-ku, Sendai 980-8578, Japan
[c] WiscSIMS, Department of Geoscience, University of Wisconsin-Madison, 1215 W Dayton St. Madison WI 53706, USA
[d] Aerospace Research and Development Directorate, Japan Aerospace Exploration Agency, Tsukuba, Ibaraki 305-8505, Japan
[e] IHI Corporation, Toyosu IHI Building, Toyosu, Koto, Tokyo 135-8710, Japan

ARTICLE INFO

Article history:
Received 6 October 2010
Received in revised form 27 June 2011
Accepted 28 June 2011
Available online 30 July 2011

Editor: R.W. Carlson

Keywords:
micrometeoroid
hypervelocity capture
international space station
transmission electron microscopy
oxygen isotopic ratios
SIMS

ABSTRACT

Here we report on the mineralogy, petrography, and oxygen-isotope compositions of a micrometeoroid captured on the international space station. This micrometeoroid has the texture of a porphyritic olivine chondrule. Because hydrated phases were not identified in the micrometeoroid and because Ni-rich sulfide in it does not show exsolution of pentlandite on the TEM scale, the micrometeoroid probably escaped low temperature events such as aqueous alteration on its parent body. However, the mean value and standard deviation of Cr_2O_3 wt.% in olivine in the micrometeoroid suggest that the micrometeoroid experienced weak thermal metamorphism. Oxygen isotope ratios of pyroxene and olivine in the micrometeoroid are similar to those of chondrule-like objects in comet 81P/Wild2 and coarse-grained crystalline micrometeorites as well as those in chondrules in major types of carbonaceous chondrites. These data suggest that the micrometeoroid is a fragment of a chondrule-like object that was derived from a primitive parent body that experienced thermal metamorphism.

1. Introduction

Once a micrometeoroid has entered the earth's atmosphere and survived atmospheric entry heating, it is usually called an interplanetary dust particle (IDP) and micrometeorite (MM). IDPs are captured by high-altitude airplanes (~20 km cruise altitude) when they are settling down in the stratosphere at a speed of ~1 cm/s (Brownlee et al., 1977). Because fine-grained (on average, ~10 μm in diameter) and/or fluffy particles descent more slowly than less porous particles, they tend to be preferentially captured by collectors that protrude from the airframe. It is thought that IDPs include particles derived from comets and asteroids (Bradley, 2004; Brownlee, 1985). On the other hand, MMs are collected by melting and filtering of Antarctic (or in some cases Arctic) ice (Maurette et al., 1991) or Antarctic snow (Duprat et al., 2007). The Antarctic MMs experienced, more or less, compaction during accumulation of snow for years and recrystallization of snow to ice. Those preserved in ice have especially experienced terrestrial weathering. Because these processes particularly damage MMs as fragile as porous and/or fluffy IDPs, most MMs are less porous and/or fluffy than IDPs. MMs are larger (typically ~100 μm in diameter) than IDPs and consist mainly of particles from hydrated asteroids (Maurette et al., 1991) although some MMs (ultracarbonaceous micrometeorites) containing abundant primitive organics may have been derived from very primitive parent bodies formed in the outer solar system (Duprat et al., 2010).

It is expected that micrometeoroids before atmospheric entry should include particles similar to both IDPs and MMs. However, the micrometeoroids captured by the Orbital debris collector (ODC)-Mir experiment on the Russian space station Mir from 1996 to 1997 are dissimilar to IDPs and MMs. Two micrometeoroids investigated by transmission electron microscope (TEM) are ~5 and ~30 μm in the longest dimension. One is composed of Fe-rich olivine (Fo_{39-50}) set in amorphous silicate material, troilite, hercynite, and chromite/magnetite, and the other is composed of Fe-rich olivine (Fo_{60-70}), magnesian high-Ca pyroxene ($Wo_{50}En_{50}Fs_0$ to $Wo_{32}En_{61}Fs_7$), and hercynite (Hörz et al., 2000). On the other hand, anhydrous IDPs, which are considered to be cometary dust, are composed mainly of sub-μm-sized components, and are typically characterized by abundant glass with embedded metal and sulfide (GEMS), enstatite whiskers, and low-iron manganese-enriched (LIME) olivine and pyroxene, as well as abundant Ni-poor pyrrhotite, and olivine and pyroxene with various Mg/(Mg + Fe) ratios (Bradley, 2004). Additionally, hydrated IDPs and

* Corresponding author at: 2-1-1 Bunkyo, Mito, Ibaraki 310-8512, Japan. Tel.: +81 29 228 8387; fax: +81 29 228 8403.
E-mail address: tngc@mx.ibaraki.ac.jp (T. Noguchi).

0012-821X/$ – see front matter © 2011 Elsevier B.V. All rights reserved.
doi:10.1016/j.epsl.2011.06.032

the majority of the least heated MMs contain abundant phyllosilicates (mainly saponite), pyrrhotite and magnetite (Maurette et al., 1991; Noguchi et al., 2002). Neither chondrules nor refractory inclusions have been identified among micrometeoroids although they have been found among the terminal captured particles from the Stardust mission to comet 81P/Wild2 (Nakamura et al., 2008; Zolensky et al., 2006) as well as MMs (Genge et al., 2005). It is not understood why the captured micrometeoroids have different mineralogy from IDPs and MMs (Hörz et al., 2000).

To test if micrometeoroids captured outside the earth's atmosphere represent fine-grained extraterrestrial material that is not sampled as IDPs and MMs, we have investigated captured particles in the silica aerogel tiles exposed to space on the international space station (ISS) that flies at about 400 km altitude. Here, we show the first micrometeoroid captured at the ISS.

2. Micrometeoroid capture by the SM/MPAC & SEED experiments

Silica aerogel, ultra-low density SiO_2 gel (~0.03 g/cm^3) was equipped on the Russian service module Zvezda on the ISS as a part of the SM/MPAC & SEED experiments implemented by Japan Aerospace Exploration Agency (JAXA) (Kimoto et al., 2009). Three identical units were exposed to space in 2001 (Fig. 1a). Silica aerogels are set in the third and fourth modules in a unit (Fig. 1b). In each unit, 24 silica aerogel tiles faced the ram side (the direction of the movement of the ISS) and the same number of silica aerogel tiles faced the wake side (the opposite side of the ram side). They are in the third and fourth trays of the SM/MPAC & SEED. Each of the tiles has a 37 × 37 mm exposure area. Each unit was retrieved from the ISS in 2002, 2004, and 2005, respectively (Kimoto et al., 2009).

3. Materials and analytical methods

Based on optical inspection of the aerogel tiles, the seven largest deceleration tracks and two largest craters (~5 to ~15 mm long) formed in the aerogel and residues in them were investigated. They are selected from all the three units of the SM/MPAC & SEED modules. Slabs of silica aerogel that contained tracks were carved out from the tiles. The thickness of the slabs is from 3 to 10 mm and depends on the line thickness of the tracks. The slab of silica aerogel tile retrieved in 2005 was cut out manually at Ibaraki University and the others were cut at Nissan Arc Co. Ltd. The terminal particle was extracted from the slab by an electric micromanipulator under a stereomicroscope in a clean bench (class 100) set in the clean room of Ibaraki University. Only one deceleration track trapped a micrometeoroid. Three tracks contain aluminum-bearing space debris. One track contains a silver-bearing particle including a 2-μm-long low-Ca pyroxene fragment, suggestive of secondary debris formed by impact of a natural particle on a man-made satellite. Residual particles could not be identified under optical microscope in two tracks and two craters.

To characterize the micrometeoroid, micro Raman spectroscopy, transmission electron microscope (TEM), field-emission scanning electron microscope equipped with energy dispersive spectrometer (FE-SEM/EDS), electron microprobe analyzer (EPMA), and secondary ion mass spectrometry (SIMS) were used. To obtain precise chemical compositions from the small areas (~2 μm in diameter) of minerals in Hoshi, we also utilized FE-EPMA JEOL JXA-8530F at Kyushu University. To decrease the X-ray excitation volume during analysis, we selected a 12 kV acceleration voltage for silicates and 15 kV for sulfide. Detection limits of SiO_2, TiO_2, Al_2O_3, Cr_2O_3, FeO, NiO, MnO, MgO, CaO, Na_2O, K_2O, and P_2O_5 are as follows: 0.06, 0.09, 0.06, 0.14, 0.17, 0.17, 0.17, 0.06, 0.11, 0.06, 0.10, and 0.12 wt.%, respectively. Those of Cr, Fe, Co, Ni, Cu, Zn, and S are as follows: 0.05, 0.06, 0.07, 0.08, 0.10, 0.14, and 0.03 wt.%, respectively. Due to the availability of the machine, FE-EPMA analyses were made after SIMS analyses.

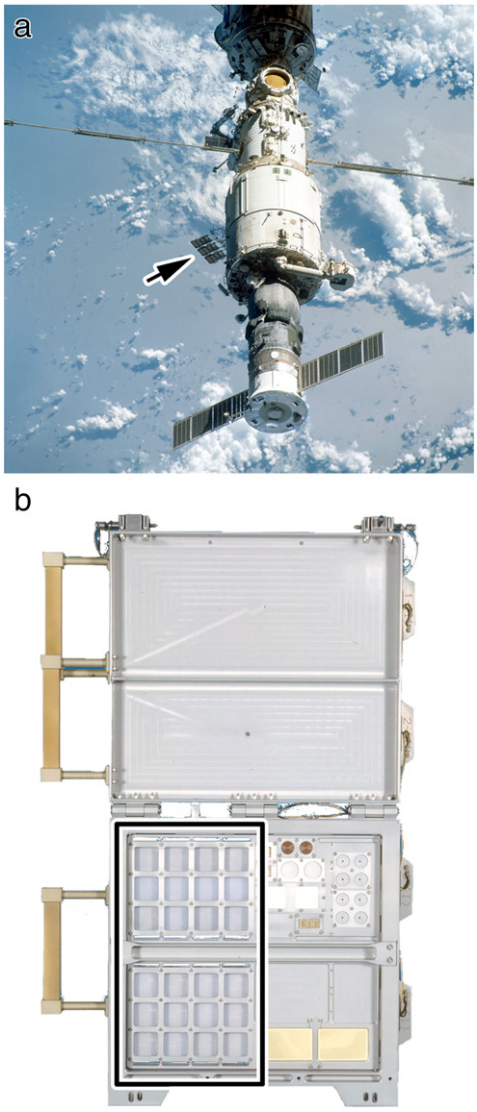

Fig. 1. (a) The service module/micro-particles capturer and space environment exposure device (SM/MPAC & SEED) equipped on the Russian service module Zvezda on the international space station (ISS) (indicated by an arrow). SM/MPAC & SEED is composed of three identical units. (b) A unit of the SM/MPAC & SEED that faced to the WAKE side (the opposite side to the direction of the movement of the ISS). Silica aerogel tiles are set on the third and fourth modules (enclosed by an open rectangle). These are copyrighted images: (a) courtesy of Roskosmos/RSC-Energia and (b) courtesy of JAXA.

We utilized JASCO NRS-3100 micro Raman spectrometer to characterize minerals in the micrometeoroid in the clean room. Excitation wavelength of the laser is 785 nm. After that, the micrometeoroid "Hoshi" was embedded in epoxy resin and ultramicrotomed into 70-nm ultrathin sections using a Reichert-Nissei Ultracut N ultramicrotome at Ibaraki University. "Hoshi" was named after the service module Zvezda, on which the SM/MPAC & SEED units were equipped, because both words hoshi and zvezda mean "star". The ultrathin sections were investigated by JEOL JEM-2000FX TEM equipped with EDAX DX4 EDS at Ibaraki University. Accelerating voltage of the TEM was 200 kV. Counting live time of EDS analysis is 100 s. Detection limits of elements investigated in this study are ~0.4 wt.%. To obtain semiquantitative elemental data of minerals in Hoshi, many natural mineral standards were used. The remainder after ultramicrotomy (potted butt) of the micrometeoroid was investigated by JEOL JSM-7000F FE-SEM/EDS and JEOL JXA-8200 EPMA at the University of Tokyo to study petrography of Hoshi.

After these analyses, the potted butt of Hoshi was embedded again with a standard for oxygen isotopic analysis by SIMS (San Carlos olivine) and cut as a 2-mm-thick epoxy disk to fit the sample holder of the SIMS. Oxygen isotope analyses of Hoshi were performed using a CAMECA 1280 SIMS at the University of Wisconsin-Madison (Kita et al., 2009; Valley and Kita, 2009). We used a focused $^{133}Cs^+$ primary beam accelerated to a total of 20 keV. The primary beam intensity was ~11 pA and 1.5 μm × 2.5 μm in size. The 10 keV secondary O^- ions were detected simultaneously by the multi-collection system with one Faraday Cup (for $^{16}O^-$) and two electron multipliers (EM, for $^{17}O^-$ and $^{18}O^-$ on an axial detector and multi-collection array, respectively). The secondary optics configuration was similar to that reported in Nakamura et al. (2008). The mass resolving powers were set to ~5000 for the axial EM detecting $^{17}O^-$ to eliminate the interference from $^{16}OH^-$ and ~2200 for the other detectors. Total analytical time per spot was about 30 min including pre-sputtering (8 min), automatic retuning of the secondary beam (2 min), and analysis (20 min). A typical count rate for $^{16}O^-$ was ~7×10^6 cps. All sample analyses were bracketed by a total of 6 spot analyses on San Carlos olivine grains ($\delta^{18}O_{VSMOW} = 5.32‰$, Kita et al., 2010) that were mounted in the epoxy disk within 1 mm from the samples in order to correct instrumental bias on the oxygen isotope ratio analyses. Pyroxene data were further corrected for matrix effects as a function of wollastonite contents (Kita et al., 2010; Valley and Kita, 2009). The typical analytical 2 SD uncertainties of bracketing standard analyses of 2 μm spot analyses were 1.2‰ in $\delta^{18}O$, 0.7‰ in $\delta^{17}O$, and 1.1‰ in $\Delta^{17}O$, respectively. These external errors are assigned as the uncertainty of the sample analyses. The contribution of OH^- interference to the $^{17}O^-$ signal was estimated using the abundance sensitivity of the ^{17}O mass spectrum at the 0.0036 amu low mass side (20 ppm) and the OH^- signal intensity monitored after every analysis. The correction was typically smaller than 0.2‰ in $\delta^{17}O$.

4. Results

4.1. Description of a deceleration track containing a micrometeoroid

A 10-mm-thick slab of silica aerogel containing the micrometeoroid "Hoshi"-bearing deceleration track was carved out from a silica aerogel tile retrieved in 2005. The deceleration track has a bulbous shape with a slender terminal portion, 14.7 mm long and 2.6 mm wide at the widest dimension (Fig. 2). The diameter of the entrance hole of the track in the aerogel is ~1.0 mm. The surface of the aerogel was brown due to contamination during exposure on the ISS (Baba and Kimoto, 2009; Steagall et al., 2009). This is the largest and longest among all the tracks found in the aerogel tiles used by the SM/MPAC & SEED experiments. The shape is similar to those of deceleration tracks found among the aerogel used in the Stardust mission except for the scarcity of fine-grained material along the track (Brownlee et al., 2006; Hörz et al., 2006). Hoshi appeared as an opaque black terminal particle having glassy luster with ~40 μm in length at the end of the track (Fig. 2). After extraction from the aerogel, a Raman spectrum of Hoshi was obtained. Two small peaks at 848 and 813 cm^{-1} were detected and interpreted to be a natural particle containing Fe-rich olivine (Kuebler et al., 2006).

4.2. Petrography and mineralogy of Hoshi

Fig. 3 is a backscattered electron (BSE) image of the remainder of Hoshi after ultramicrotomy. It has a microporphyritic texture and contains abundant low-Ca pyroxene microphenocrysts (less than 15 μm in diameter). Low-Ca pyroxene microphenocrysts are truncated at the edge of this igneous object showing that it is a fragment of larger object (Fig. 3). Olivine microphenocrysts have rounded shapes and are less than 10 μm in diameter. Low-Ca pyroxene has relatively homogeneous chemical compositions [$Wo_{3.1}En_{85.3}Fs_{11.6}$ on average] (Fig. 4a). Olivine

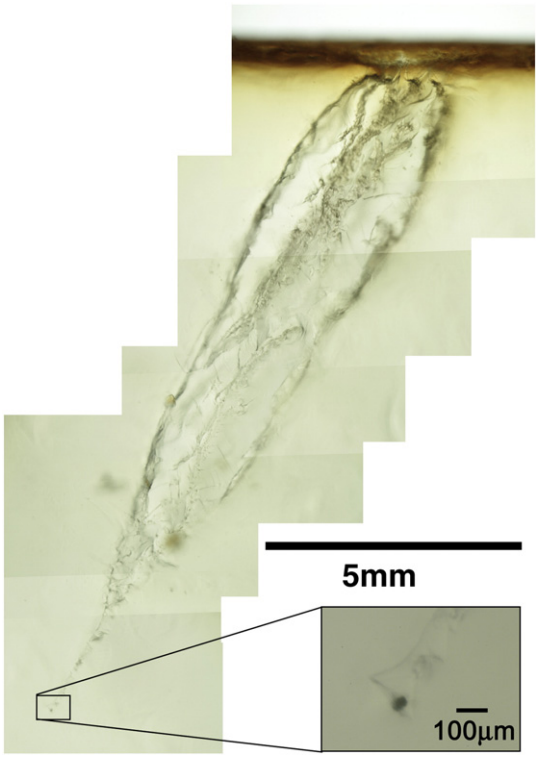

Fig. 2. An optical image of a large deceleration track found in an aerogel tile retrieved in 2005 from the international space station. This is the largest and longest (14.7 mm) track found among all the aerogel tiles used in the SM/MPAC and SEED experiments performed from 2001 to 2005. Inset shows an enlarged image of the terminus of the track with an opaque black particle ~40 μm in length. The surface of the aerogel tile is brown, which appeared as dark gray in this black and white figure, due to contamination formed during exposure on the ISS.

phenocrysts have relatively FeO-rich chemical compositions [$Fo_{79.3}$ on average] except for olivine rimming a large (~7 μm × 3 μm) Ni-rich pyrrhotite inclusion [$Fo_{63.5}$] (Figs. 3, 4a). MnO content of olivine is fairly homogeneous (0.72–0.77 wt.%) although FeO content of olivine ranges from 15.02 to 30.32 wt.%. Fig. 5a shows that Mn/Fe molar ratios of

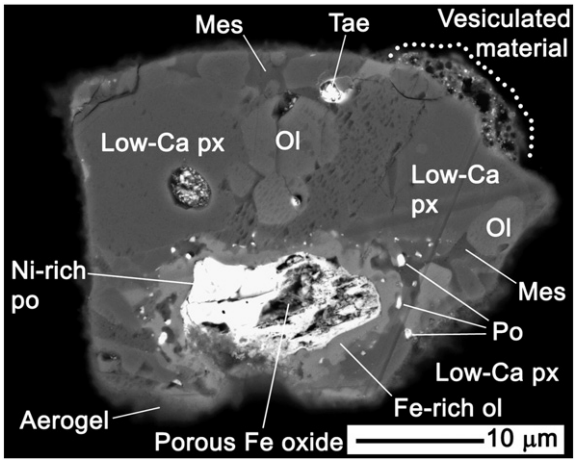

Fig. 3. Backscattered electron (BSE) image of the terminal particle Hoshi after ultramicrotomy. It has a microporphyritic texture and is composed mainly of low-Ca pyroxene, olivine, Ni-rich pyrrhotite, porous Fe oxide, and interstitial glass. Vesiculated material is indicated by a dotted curve. It was formed during capture in silica aerogel. Abbreviations: Ol, olivine; Low-Ca px, low-Ca pyroxene; Mes, mesostasis; Po, pyrrhotite; Tae, taenite.

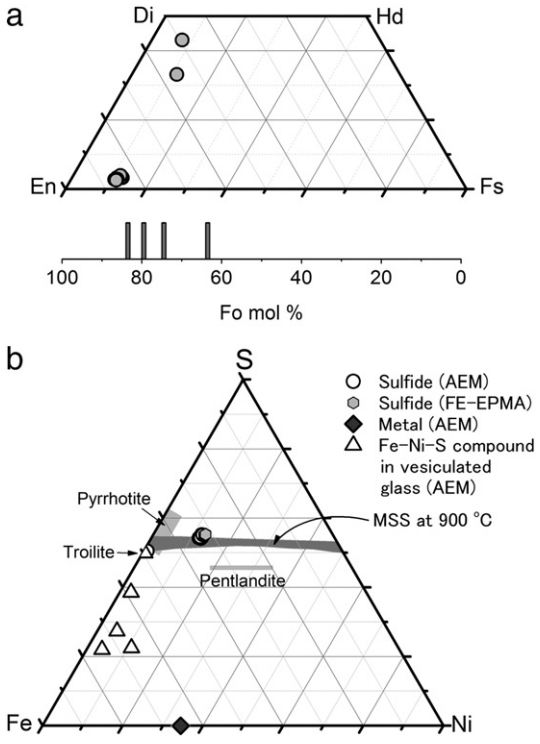

Fig. 4. Compositions of (a) pyroxene and olivine and (b) Fe–Ni sulfides, Fe–Ni metal, and Fe–Ni–S compound in Hoshi. Low-Ca pyroxene in Hoshi has relatively homogeneous chemical compositions. The large (~10 μm across) inclusion in Fig. 3 contains is Ni-rich sulfide. It has homogeneous chemical composition equivalent to monosulfide solid solution (mss). One of the small sulfide grains around the sulfide-oxide inclusion was Ni-poor pyrrhotite. Round shaped inclusions of Fe–Ni–S (Fe–Ni–S compound) in vesicular glass on the surface of Hoshi are depleted in S to various degrees, which is similar to that among the Stardust samples. The field of mss at 900 °C (Raghavan, 2004) is displayed in Fig. 4b. Chemical compositions of olivine, orthopyroxene, and Ni-rich sulfide were measured by field emission electron microprobe (FE-EPMA). High-Ca pyroxene, Ni-poor pyrrhotite, and Fe–Ni–S compound were measured by energy dispersive spectrometer equipped on a transmission electron microscope (AEM).

olivine are similar to or higher than those of olivine in type IIA chondrules in ordinary chondrites with petrologic subtypes ≤3.05, and much higher than those in CO chondrites with petrologic subtypes ≤3.2 (Berlin et al., 2011). There is a positive correlation between molar Fe/Mn ratio and molar Fe/Mg ratio of olivine (Fig. 5b). In both Fig. 5a and b, one point is plotted near the best-fit linear regression lines of olivine in ordinary chondrites. It corresponds to olivine overgrown on Ni-rich pyrrhotite. In some olivine crystals small amounts of Cr_2O_3 were detected (0.13–0.19 wt.%). Mean Cr_2O_3 and standard deviation of Cr_2O_3 content in olivine plot near the fields of ordinary chondrites with petrologic subtype ≥3.2 and of Kainsaz and Rainbow CO3.2 chondrites (Grossman and Brearley, 2005), indicative of weak thermal metamorphism (Fig. 5c).

Because Hoshi is enclosed by dark materials, it is not clear whether the interstitial material among microphenocrysts of olivine and pyroxene is optically isotropic or cryptocrystalline under an optical microscope. Although it was also difficult to identify crystallites in the interstitial material in BSE images, sub-micrometer-sized plagioclase was identified in the interstitial material by TEM. Therefore, we call the interstitial material as mesostasis. When the ranges of SiO_2, Al_2O_3, FeO, MgO, CaO, and Na_2O wt.% in the mesostasis are compared with those in type I (molar Fe/(Mg + Fe) in olivine and pyroxene ≤ 10%) and type II (molar Fe/(Mg + Fe) in olivine and pyroxene > 10%) chondrules in CO3.0 and 3.2 and those in Semarkona LL3.0 chondrite (Jones, 1990, 1992, 1994; Jones and Scott, 1989; Rubin and Wasson, 1988) (Fig. 5d), all the items are within the range of type I chondrules. This means that the mesostasis has an anorthite-rich feldspathic composition. The large Ni-rich pyrrhotite inclusion is partially replaced by porous Fe oxide and is enclosed by olivine (Fig. 3). The inclusion is surrounded by the mesostasis. Fine-grained (<2 μm in diameter) Ni-poor pyrrhotite [$Fe_{49}Ni_1S_{50}$] and taenite are dispersed in the mesostasis around the large Ni-rich pyrrhotite inclusion (Fig. 3, Table 1).

On the upper right edge of Hoshi, vesiculated material is attached on the surface of the igneous object (Fig. 3). It is composed of vesicular glass with embedded round-shaped inclusions of a Fe–Ni–S compound, which is similar to grains in silica aerogel captured by the Stardust mission and formed by mixing and melting of the surface of the impactor and silica aerogel during hyper velocity capture in silica aerogel (Brownlee et al., 2006; Zolensky et al., 2006). The round shaped inclusions of Fe–Ni–S are depleted in S to various degrees; this is also common to the Stardust samples (Zolensky et al., 2006).

Minor phases that can be identified only by TEM are high-Ca pyroxene with variable Wo contents (Fig. 4a), 200 to 400-nm-long grains of Ca-rich plagioclase [$An_{82}Ab_{18}$ on average] (Fig. 6a, Table 1), and rare 100-nm diameter chrome-rich spinel, all of them are found in the mesostasis although they could not be identified in BSE images of the mesostasis. We could not find aqueous alteration products such as phyllosilicates in all the minerals observed by TEM.

Lattice images and selected area electron diffraction (SAED) patterns of low-Ca pyroxene in Hoshi show that it is composed of orthopyroxene with 1.8-nm (100) lattice fringes normal to the a^* direction with stacking disorder normal to the [100]* direction (Fig. 6b).

The large Ni-rich sulfide shown in Figs. 3 and 6a is compositionally homogeneous monosulfide solid solution (mss) [$Fe_{33}Ni_{12}S_{55}$ on average] (Fig. 4b; Table 1). However, structurally this phase is pyrrhotite showing subsidiary diffraction spots consistent with the a = 2A, c = 3C superstructure, which has the three fold lattice periodicity of the basic pyrrhotite structure along the c^* direction (Fig. 7d). The sulfide grain is partially oxidized to iron oxide (Fig. 7a). The SAED pattern of the iron oxide indicates that it is magnetite with unusual three-fold superstructure diffraction spots along the [111]* direction (Fig. 7c). A high resolution TEM image of magnetite reveals that it contains 20- to 30-nm thick regions of both normal magnetite and the unusual magnetite with a three-fold superstructure along the [111]* direction (Fig. 7b). The latter regions are the cause of the superstructure diffraction spots, possibly related to ordered vacancies.

4.3. Oxygen isotope ratios of ferromagnesian silicates in Hoshi

We obtained seven O isotope analyses of olivine and low-Ca pyroxene in Hoshi (Fig. 8; Table 2). A total of seven spot analyses were obtained mainly from low-Ca pyroxene, except for one pit that hit an olivine phenocryst at the center. The $\delta^{18}O$ value of olivine (1.4‰) is somewhat lower than those of pyroxene (average 2.4 ± 0.2‰), but all data including the $\delta^{17}O$ and $\Delta^{17}O$ values are indistinguishable within analytical uncertainties (Table 2). The average $\Delta^{17}O$ value of Hoshi is −1‰ (Table 2). They plot below the terrestrial fractionation (TF) line, and between the TF line and the carbonaceous chondrite anhydrous mineral (CCAM) line (Clayton, 1993). They are within the fields of the 81P/Wild2 cometary particles (McKeegan et al., 2006; Nakamura et al., 2008), anhydrous IDPs (Aléon et al., 2009; Engrand et al., 1999a; Nakashima et al., 2011), and coarse-grained crystalline Antarctic MMs (AMMs) (Engrand et al., 1999b; Gounelle et al., 2005) (Fig. 8). The compositions of these fields are very similar to those of ferromagnesian silicates in chondrules of carbonaceous chondrites (Clayton, 1993; Yurimoto et al., 2008; Krot et al., 2010). On the other hand, the fields of ferromagnesian silicates in chondrules of ordinary, enstatite, and Rumuruti chondrites (Clayton et al., 1991; Greenwood et al., 2000; Kita et al., 2008; 2010; Weisberg et al., 2010) are above the TF line.

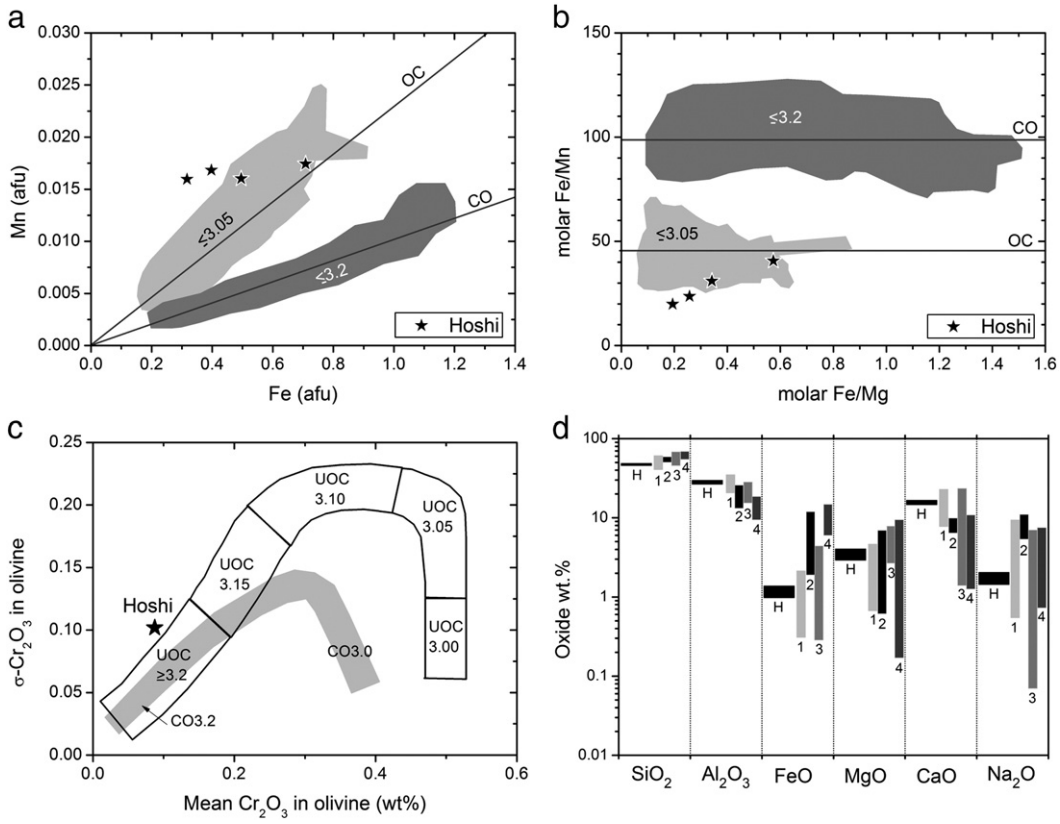

Fig. 5. (a) Mn versus Fe (afu = atomic formula units based on four oxygen atoms) diagram for individual analyses of olivine in Hoshi. This figure also shows best-fit linear regressions for olivine in type II chondrules in ordinary chondrites (OC) and CO chondrites (CO) from the origin and fields of individual analyses. These data are from Berlin et al. (2011). (b) Molar Fe/Mn versus molar Fe/Mg diagrams for individual analyses of olivine in Hoshi. Averaged Fe/Mn ratios and field of individual analyses (Berlin et al., 2011) are also displayed. (c) Standard deviation versus mean value of the Cr_2O_3 content of olivine in Hoshi. Fields of olivine in UOC and CO chondrites obtained by Grossman and Brearley (2005) are also displayed. (d) Comparison of chemical composition of mesostasis in Hoshi with those in glass or mesostasis in type I and II chondrules in UOC and CO chondrites (Jones, 1990, 1992, 1994; Jones and Scott, 1989; Rubin and Wasson, 1988). 1, type I in UOC; 2, type II in UOC; 3 type I in CO; 4; type II in CO.

5. Discussion

5.1. Structure of the precursor of Hoshi

The diameter of the entrance hole of the track, ~1.0 mm, is 25 times larger in diameter than the diameter of the particle (~40 μm). The ratio between the particle and the entrance hole (~0.04) is similar to the ratios of diameters of the chondrules and the entrance holes in the cases of the Stardust chondrules (~0.03) (Nakamura et al., 2008). Because the shape of the track is bulbous and similar to many Stardust tracks (Hörz et al., 2006), as well as experimental tracks formed by a mixture of glass beads embedded in cocoa powder to simulate the

Table 1
Representative analyses of minerals in Hoshi.

Mineral	Average olivine (n = 3)	Olivine enclosing pyrrhotite	Average low-Ca pyroxene (n = 14)	Average glass (n = 4)	High-Ca pyroxene	Average plagioclase (n = 4)	Average vesicular glass (n = 3)		Taenite	Ni-rich pyrrhotite	Average Ni-rich pyrrhotite (n = 4)	Pyrrhotite
FE-EPMA/AEM	FE-EPMA	FE-EPMA	FE-EPMA	FE-EPMA	AEM	AEM	AEM	FE-EPMA/AEM	AEM	AEM	FE-EPMA	AEM
SiO_2	39.31	36.15	55.02	47.42	51.65	46.91	60.48	Cr	n. a.	n. a.	0.07	n. a.
TiO_2	b. d.	b. d.	0.12	b. d.	0.72	b. d.	b. d.	Fe	64.31	42.40	39.43	61.86
Al_2O_3	b. d.	b. d.	1.74	28.06	3.76	33.72	2.56	Co	n. a.	n. a.	0.68	n. a.
Cr_2O_3	0.12	b. d.	1.08	0.13	1.71	b. d.	0.67	Ni	35.69	16.48	16.85	1.18
FeO	18.70	40.30	7.45	1.24	6.78	0.22	7.87	Cu	n. a.	n. a.	0.43	n. a.
MnO	0.75	b. d.	0.43	b. d.	0.93	b. d.	0.71	S	b. d.	41.12	39.24	36.96
MgO	40.30	29.63	30.76	3.57	18.86	b. d.	22.01	Total wt.%	100.00	100.00	96.71	100.00
CaO	0.17	0.29	1.58	15.82	15.61	17.04	1.69					
Na_2O	b. d.	b. d.	b. d.	1.77	b. d.	2.11	b. d.					
K_2O	b. d.	b. d.	b. d.	b. d.	b. d.	b. d.	b. d.					
SO_3	b. d.	b. d.	b. d.	b. d.	b. d.	b. d.	4.01					
Total wt.%	99.33	97.13	98.18	98.20	100.00	100.00	100.00					
Mg/(Mg + Fe)	0.793	0.635	0.88	0.84	0.83	–	0.83					
	$Fo_{79.3}$	$Fo_{63.5}$	$Wo_{3.1}En_{85.3}$ $Fs_{11.6}$		$Wo_{33}En_{56}$ Fs_{11}	$An_{82}Ab_{18}$ Or_0						

n. a. means “not analyzed”.
b. d. means “below detection”.

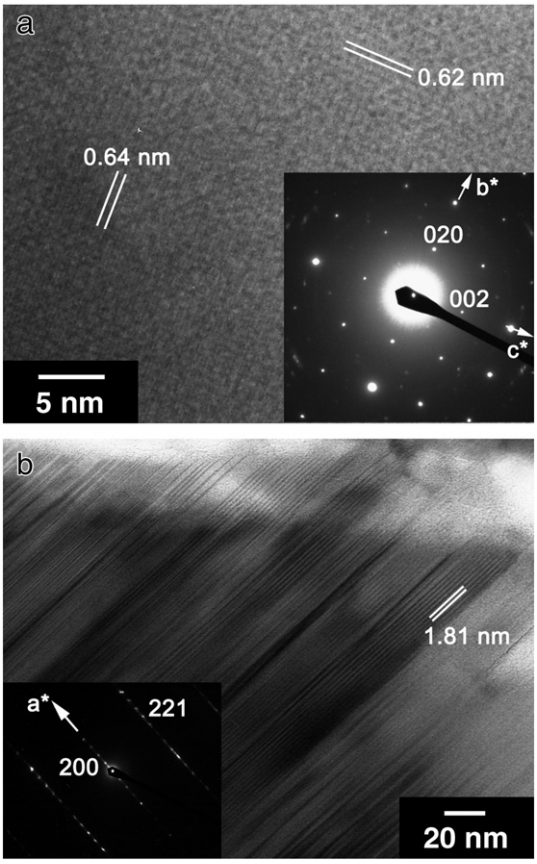

Fig. 6. (a) Bright-field TEM image of plagioclase in mesostasis. Lattice fringes and the selected area electron diffraction (SAED) pattern indicate that it is well-crystalline. (b) Bright-field TEM image of low-Ca pyroxene in Hoshi. Lattice fringes (mainly 1.8 nm along the a* direction) and selected area electron diffraction (SAED) pattern indicate that it is orthopyroxene containing stacking faults.

shapes of some of the Stardust deceleration tracks (Hörz et al., 2006), the precursor of Hoshi may have been composed of a coarse-grained "hard" particle embedded in fragile fine-grained material like some Stardust samples (Hörz et al., 2006).

5.2. Hoshi as a fragment of a chondrule-like object

Chondrules are the major components of chondritic meteorites and are usually submillimeter-sized igneous objects that floated in free space before incorporation in meteorites. Most chondrules are composed of ferromagnesian silicates such as olivine and pyroxene as well as feldspathic glass and show evidence for partial or complete melting (Brearley and Jones, 1998; Lauretta et al., 2006). To identify an object as a chondrule, we have to find the evidence that the object was incorporated in the host material after crystallization of the object. Direct contact of an igneous object with fine-grained material like chondrite matrix is circumstantial evidence that the object is a chondrule or a chondrule fragment. Although the object found in this study has igneous texture, we could not find fine-grained matrix attached directly to the igneous object. Therefore, it is difficult to prove that Hoshi is a chondrule. However, Hoshi has microporphyritic texture that resembles a porphyritic olivine pyroxene (POP) chondrule, ferromagnesian mineralogy that also resembles that of POP chondrules, and oxygen isotopic ratios of the ferromagnesian silicates are within the range of these minerals in chondrules in carbonaceous chondrites as well as crystalline MMs and Wild2 particles. Therefore, we conclude that the igneous object Hoshi could be called as a chondrule-like object.

Low-Ca pyroxene in Hoshi is orthopyroxene (Fig. 5b). Primary orthopyroxene-bearing chondrules are minor but have been reported from some chondrites such as Semarkona LL3.0 chondrite (Brearley and Jones, 1998) and ALH 85085 CH chondrite (Brearley, 1990) as well as terminal particles in the Stardust samples (Jacob et al., 2009). Primary orthopyroxene has higher Wo contents (Wo_{2-4}) than clinoenstatite that was transformed from protoenstatite ($<Wo_{1.5}$). High Ca content of orthopyroxene (Wo_3) in Hoshi indicates that it is a primary phase crystallized from a melt (Fig. 4a, Table 1). Average Al_2O_3 and Cr_2O_3 contents of the orthopyroxene in Hoshi (1.74 and 1.08 wt.%, respectively, Table 1) also support that it is primary orthopyroxene because Al_2O_3 and Cr_2O_3 wt.% of low-Ca clinopyroxene do not exceed 1.5 and 1 (Brearley and Jones, 1998).

Fe–Mn systematics of type IIA chondrules in the least metamorphosed CO, CR, and unequilibrated ordinary chondrites (UOC) show that olivine data in CO and UOC can be fit on lines from the origin on the Fe versus Mn diagram and that those in CR plot between these lines (Berlin et al., 2011). Berlin et al. (2011) also found that relict olivine grains have significantly different Fe/Mn ratios from those of the host chondrule olivine in Kainsaz CO3.2. In the case of Hoshi, there is a trend between microphenocrystic olivine and FeO-rich olivine overgrown on the sulfide-Fe oxide inclusion in the Fe versus Mn diagram (Fig. 5a). Because the averaged Cr_2O_3 contents and their variations of olivine suggest that weak thermal metamorphism affected Hoshi (Fig. 5b), this trend was probably formed during incomplete homogenization between the microphenocrysts and the overgrowth. Although olivine in Hoshi experienced weak thermal metamorphism, Mn afu in phenocrystic olivine would not have changed considerably during metamorphism because the Mn of olivine overgrowth is similar to that of the olivine microphenocrysts. The most magnesian olivine in Hoshi has 0.19 M Fe/Mg and 19.85 M Fe/Mn, which are comparable with those in Torajiro, a chondrule-like object found among the Wild2 particles (the averaged values: 0.26 and 23.49, respectively) (Nakamura et al., 2008). Because pyroxene does not exchange Fe and Mg cations as fast as olivine does (e. g. Ganguly and Tazzoli, 1994), Mg/(Mg + Fe) atomic ratio of orthopyroxene may have not been considerably changed during weak thermal metamorphism. By considering Mg/(Mg + Fe) atomic ratios in olivine and orthopyroxene in UOCs (Jones, 1996), Mg/(Mg + Fe) atomic ratio of the olivine microphenocrysts in Hoshi when they crystallized may have been around 0.85, Fe/Mn ratio of olivine before thermal metamorphism may have been even higher than that in Torajiro.

Fe-sulfides are rare among type I chondrules, but are abundant in type II chondrules. They have been reported from type II chondrules in Semarkona LL3.0 chondrite (Jones, 1990) and some CR chondrites (Schrader et al., 2008), agglomeratic olivine chondrules in Semarkona (Weisberg and Prinz, 1994), and a type II chondrule-like object Iris retrieved from 81P/Wild2 comet (Gainsforth et al., 2010). Hoshi resembles type II chondrules in terms of abundance of sulfide. However, because Hoshi experienced weak thermal metamorphism, it is not clear if Hoshi resembles type II chondrules when it crystallized.

Magnetite-sulfide-metal inclusions in chondrules have been reported as alteration products from CV chondrites (e. g. Haggerty and McMahon, 1979). FeO-rich olivine haloes have been also reported around such inclusions in CV chondrites (Brearley and Jones, 1998). However, in CV chondrites, sulfides in the magnetite-bearing complexes are troilite or both troilite and pentlandite. On the other hand, the sulfide-Fe oxide inclusion in Hoshi contains sulfide with a chemical composition of mss (Fig. 4b, Table 1). Magnetite partially replacing the sulfide shows superstructure diffraction spots (Fig. 6). Magnetite and sulfide-bearing inclusions with these characteristics have not been reported from CV chondrites as well as the other carbonaceous chondrites to date.

As shown in Fig. 4b, Ni-rich pyrrhotite is homogeneous on micrometer to sub-micrometer scales [average FE-EPMA data is $Fe_{31.9}Ni_{13.0}S_{55.2}$; average AEM data is $Fe_{33}Ni_{12}S_{55}$]. Based on Fe–Ni–S phase diagrams

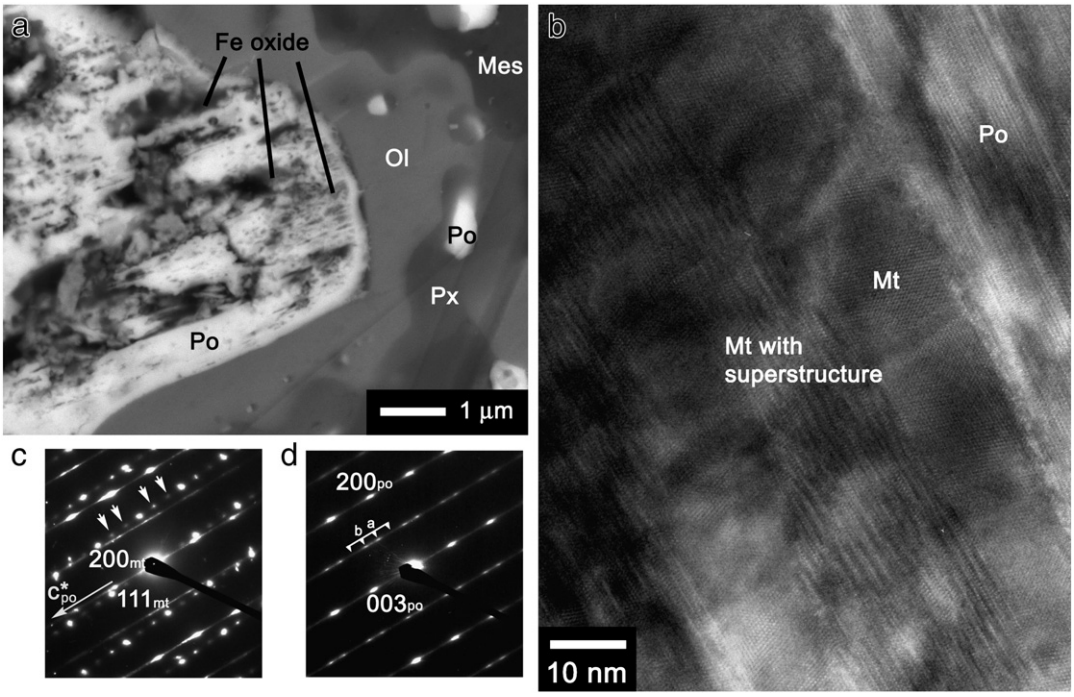

Fig. 7. (a) An enlarged BSE image of the Ni-rich pyrrhotite–Fe oxide inclusion. The Ni-rich pyrrhotite is partially replaced by magnetite and enclosed by Fe-enriched (Fo_{57-62}) olivine in Fig. 3. Iron oxide regions seem to have been fragile; their structure was partly destroyed during sectioning for TEM and polishing for SIMS. Abbreviations: Po, pyrrhotite, Ol, olivine, Px, pyroxene, Mes, mesostasis. (b) High resolution TEM image of a boundary between Ni-rich pyrrhotite and iron oxide. Mt, magnetite. (c) SAED pattern of the area in Fig. 6b. The c^* direction of pyrrhotite (c^*_{po}) is oblique to the $[111]^*$ direction of magnetite ($[111]^*_{mt}$), which corresponds to their boundary in Fig. 6(b). The SAED of magnetite shows a 3-fold superstructure along the $[111]^*_{mt}$ direction, which corresponds to the areas with the 3-fold superstructure in Fig. 6(b). The superstructure areas may be related to ordered vacancies. (d) SAED pattern of Ni-rich pyrrhotite in the inclusion. Subsidiary reflection spots labeled "a" and "b" indicate the three-fold reciprocal lattice periodicity along the c^* direction of pyrrhotite.

(Raghavan, 2004), mss with the composition $Fe_{32-33}Ni_{13-12}S_{55}$ exsolves pyrite at temperatures around ~600 °C (Raghavan, 2004). The chemical composition of the Ni-rich pyrrhotite suggests that the sulfide crystallized as mss probably from S-bearing Fe–Ni melt or that it was formed by sulfidation of Ni-rich metal at temperatures where mss is stable. The latter interpretation is supported by the Co/Ni wt.% ratio in the Ni-rich pyrrhotite 0.04 is similar to the CI chondritic (solar) Co/Ni ratio 0.05 (e.g., Anders and Grevesse, 1989). If the sulfide-metal-oxide assemblage were formed during weak thermal metamorphism cooling rate after heating must have been enough rapid not to exsolve pyrite from Ni-rich pyrrhotite.

Magnetite in the inclusion has superstructure reflections, which have been reported only from a unique cosmic symplectite (COS) in Acfer 094 carbonaceous chondrite (Sakamoto et al., 2007). However, COS is composed of sub-μm-sized mixtures of pentlandite and magnetite and set in the matrix and the magnetite in the COS has three-fold superstructure reflections along all the {111}* directions (Sakamoto et al., 2007; Seto et al., 2008). If oxidation of pyrrhotite to magnetite occurred after exsolution of pentlandite from mss in the COS, magnetite must have been formed at temperatures lower than ~100 °C (Brearley and Martinez, 2010). On the cometary, in case of Hoshi, oxidation at temperatures higher than ~600 °C and subsequent rapid cooling are estimated based on the absence of exsolution in the Ni-rich sulfide. Structural differences of magnetite in Hoshi and that in COS may reflect these different formation temperatures.

Formation of the FeO-enriched olivine around the Ni-rich sulfide-Fe oxide inclusion must have also occurred at temperatures higher than ~600 °C. A positive correlation between molar Fe/Mg and molar Fe/Mn in olivine (Fig. 5b) is consistent with addition of Fe by oxidation of the Ni-rich sulfide (e. g. Berlin et al., 2011). Weak thermal metamorphism suggested by the mean value and standard deviation of Cr_2O_3 in olivine (Fig. 5c) may have enhanced exchange of the added Fe cations with Mg and Mn cations in olivine and subsequent increases of both Fe/Mg and Fe/Mn ratios in olivine (Fig. 5b). If sulfidation occurred during thermal metamorphism, sulfidation of Ni-rich metal, oxidation of the sulfide, and formation of FeO-rich olivine halo around the sulfide-oxide inclusion may have occurred at approximately the same time.

5.3. Estimation of the parent body of Hoshi

Mss has been also reported from CR and CM chondrites. Mss in chondrules in CR chondrites shows exsolution lamellae of pentlandite up to ~20 μm thick (Schrader et al., 2010). Ni-rich sulfide has been identified also in CM chondrites and it contains submicron exsolution of pentlandite (Brearley and Martinez, 2010). The Ni-rich sulfide in chondrules in these meteorites is considered to have been mss when it crystallized during chondrule formation (at least, in case of CR chondrites) and pentlandite is considered to occur an exsolved phase from mss during aqueous alteration on CR and CM parent bodies (Brearley and Martinez, 2010; Schrader et al., 2010). Because sub-μm-sized exsolution of pentlandite from mss could occur below 100 °C on a time scale of several tens of thousands years (Brearley and Martinez, 2010), it is likely that Hoshi must have cooled from temperatures higher than ~600 °C to those well below 100 °C within a time scale much shorter than several tens of thousands years. Because oxygen isotopic compositions of ferromagnesian silicates in Hoshi are near the higher end of the range of 81P/Wild2 comet, anhydrous IDPs, and coarse-grained crystalline Antarctic MMs (AMMs), as well as chondrules in carbonaceous chondrites (Fig. 8), the precursor of Hoshi was formed from an oxygen isotope reservoir common to the above-mentioned solar system materials. Therefore, the parent body of Hoshi may be a primitive asteroid that experienced weak thermal metamorphism.

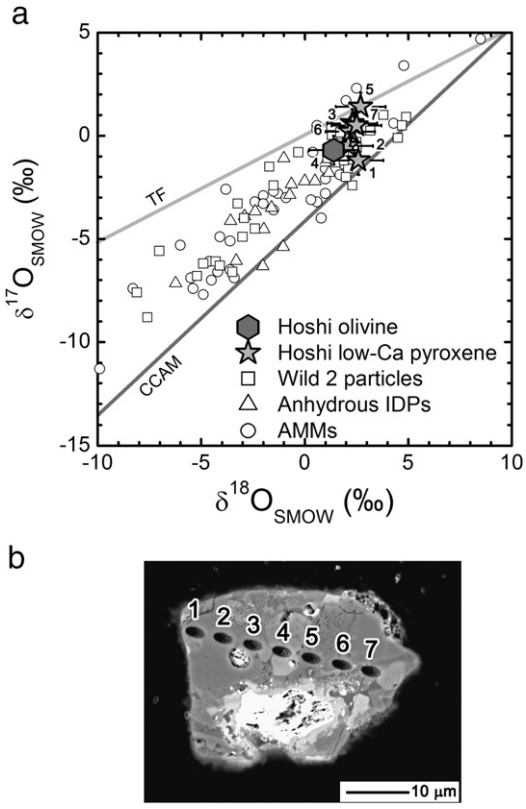

Fig. 8. (a) Oxygen three-isotope ratios of olivine and low-Ca pyroxene. Compositions of Wild 2 chondrule-like objects (McKeegan et al., 2006; Nakamura et al., 2008), anhydrous interplanetary dust particles (IDPs) (Aléon et al., 2009), and coarse-grained crystalline Antarctic micrometeorites (AMMs) (Engrand et al., 1999a,b; Gounelle et al., 2005) are also shown for comparison. The isotope ratios plot below the terrestrial fractionation (TF) line and above the carbonaceous chondrite anhydrous mixing (CCAM) line. (b) BSE image showing spots analyzed with ion microprobe for oxygen isotope ratios. Seven spots were analyzed using a 2-μm diameter Cs^+ beam. Numbers in this BSE correspond to those in (a).

5.4. A possible cause of the dissimilarity of the Mir micrometeoroids to IDPs and MMs

Although the numbers of the ISS chondrule-like object (n = 1) and the Stardust chondrule-like objects (n = 4) (Nakamura et al., 2008) are small at present, the proportions of FeO-rich chondrule-like objects among them (collectively 40%) seems to be higher than the proportion of type II chondrules for the major types of carbonaceous chondrites (<1% to ~5%) (Brearley and Jones, 1998; Schrader et al., 2008) but similar to those for Acfer 094 (25%), Y81020 CO 3.0 (20%), and QUE97990 CM2 (20%) (Kunihiro et al., 2005). However, it is beyond the scope of this paper to discuss the reason why these meteorites contain a higher amount of type II chondrules. As already mentioned, two micrometeoroids captured on the Mir space station are composed of Fe-rich olivine, troilite, two spinels embedded in amorphous silicate material, and of Fe-rich olivine, high-Ca pyroxene, and hercynite (Hörz et al., 2000). If the population of Mir micrometeoroids containing olivine with >10% molar Fe/(Mg + Fe) were as high as those of the ISS and the Stardust chondrule-like objects, it could be possible that both of the Mir micrometeoroids investigated by TEM (Hörz et al., 2000) contain FeO-bearing olivine. The absence of micrometeoroids similar to IDPs and MMs composed mainly of sub-μm-sized components may have resulted from selective destruction during capture in silica aerogel as is the case in the Stardust samples (Hörz et al., 2000; Zolensky et al., 2006). These could be the reasons that micrometeoroids captured at the Mir space station are dissimilar to both IDPs and MMs.

Acknowledgements

We appreciate IHI Aerospace Co. Ltd., Advanced Engineering Services Co. Ltd., and Nissan Arc Co. Ltd. for supporting the optical inspection of the silica aerogel tiles. We thank H. Nagahara and H. Yoshida for permission to use FE-SEM and EPMA at University of Tokyo. We thank K. Shimada, K. Sakamoto and R. Okazaki, for making it possible for us to perform FE-EPMA analysis at Kyushu University. We appreciate M. Kimura's comments on opaque mineralogy of chondrules. Constructive comments by two anonymous reviewers helped to improve our manuscript considerably. This work is supported by NASA grants NNX07AI46G and NNX09AC30G (N.K.) and by a Grant-in-aid of the Japan Ministry of Education, Culture, Sports, Science and Technology (17340157) to T. Noguchi. WiscSIMS is supported partly by NSF (EAR03-19230 and EAR07-44079). The machine fee was supported by a Grant-in-aid of the Japan Ministry of Education, Culture, Sports, Science and Technology (19104012) to T. Nakamura.

References

Aléon, J., Engrand, C., Leshin, L.A., McKeegan, K.D., 2009. Oxygen isotopic composition of chondritic interplanetary dust particles: a genetic link between carbonaceous chondrites and comets. Geochim. Cosmochim. Acta 73, 4558–4575.
Anders, E., Grevesse, N., 1989. Abundances of the elements: Meteoritic and solar. Geochim. Cosmochim. Acta 53, 197–214.
Baba, N., Kimoto, Y., 2009. Contamination growth observed on the micro-particles capturer and space environment exposure device. J. Spacecraft Rockets 46, 33–38.
Berlin, J., Jones, R.H., Brearley, A.J., 2011. Fe–Mn systematics of type IIA chondrules in unequilibrated CO, CR, and ordinary chondrites. Meteorit. Planet. Sci. 46, 513–523.
Bradley, J.P., 2004. Interplanetary dust particles. In: Davis, A.M. (Ed.), Treatise in Geochemistry. Elsevier-Pergamon, pp. 689–711.

Table 2
Oxygen three-isotope ratios measured by ion microprobe from 2-micrometer spots.[a]

Mineral	SIMS spot	$\delta^{18}O$ ‰	2SD ‰	$\delta^{17}O$ ‰	2SD ‰	$\Delta^{17}O$ ‰	2SD ‰	OH cor ‰[b]
Low-Ca pyroxene	1	2.6	1.2	−1.2	0.7	−2.6	1.1	1.2
Low-Ca pyroxene	2	2.1	1.2	−0.5	0.7	−1.6	1.1	0.2
Low-Ca pyroxene	3	2.3	1.2	0.6	0.7	−0.6	1.1	0.1
Olivine	4	1.4	1.2	−0.7	0.7	−1.4	1.1	0.1
Low-Ca pyroxene	5	2.7	1.2	1.4	0.7	0.0	1.1	0.1
Low-Ca pyroxene	6	2.2	1.2	0.2	0.7	−0.9	1.1	0.2
Low-Ca pyroxene	7	2.5	1.2	0.5	0.7	−0.8	1.1	0.2
Average[c]	2–7	2.2	0.9	0.3	1.5	−0.9	1.1	

[a] Data are corrected for instrumental biases and a contribution of tailing from hydride (^{16}OH) peak on ^{17}O. The uncertainties of individual analyses are estimated from spot-to-spot reproducibility (2SD) of standard olivine analyses (n = 6) in the same epoxy disk, though those associated from hydride corrections are not included.
[b] Hydride ^{16}OH interference correction factors on the ^{17}O signals, which corresponds to 20 ppm of ($^{16}OH/^{17}O$) signal ratios at the end of individual analyses.
[c] The average value and 2SD from 6 analyses (except for spot-1 with a relatively larger hydride correction).

Brearley, A.J., 1990. Constraints on the shock and thermal histories of some components from the unique chondrite, Allan Hills 85085, and their implications. Lunar Planet. Sci. XXI, 123–124.
Brearley, A.J., Jones, R., 1998. Chondritic meteorites. In: Papike, J.J. (Ed.), *Planetary materials*, *Reviews in Mineralogy*, 36. Mineralogical Society of America. p. 3:1-370.
Brearley, A.J., Martinez, C., 2010. Ubiquitous exsolution of pentlandite and troilite in pyrrhotite from the TIL 91722 CM2 carbonaceous chondrite: a record of low temperature solid state processes. Lunar Planet. Sci. XXXXI (CD #1689).
Brownlee, D.E., 1985. Cosmic dust—collection and research. Annu. Rev. Earth Planet. Sci. 13, 147–173.
Brownlee, D.E., Tomandl, D.A., Olszewski, E., 1977. Interplanetary dust: a new source of extraterrestrial material for laboratory studies. Proc. 8th Lunar Sci. Conf, pp. 149–160.
Brownlee, D.E., et al., 2006. Comet 81P/Wild 2 under a microscope. Science 314, 1711–1716.
Clayton, R.N., 1993. Oxygen isotopes in meteorites. Ann. Rev. Earth Planet. Sci. 21, 115–149.
Clayton, R.N., Mayeda, T.K., Olsen, E.J., Goswami, J.N., 1991. Oxygen isotope studies of ordinary chondrites. Geochim. Cosmochim. Acta 55, 2317–2337.
Duprat, J., et al., 2007. Micrometeorites from Central Antarctic snow: the CONCORDIA collection. Adv. Space Res. 39, 605–611.
Duprat, J., et al., 2010. Extreme deuterium excesses in ultracarbonaceous micrometeorites from Central Antarctic snow. Science 328, 742–745.
Engrand, C., McKeegan, K.D., Leshin, L.A., Bradley, J.P., Brownlee, D.E., 1999a. Oxygen isotopic compositions of interplanetary dust particles: ^{16}O-excess in a GEMS-rich IDP. Lunar Planet. Sci. XXX (#1690).
Engrand, C., McKeegan, K.D., Leshin, L.A., 1999b. Oxygen isotopic compositions of individual minerals in Antarctic micrometeorites: further links to carbonaceous chondrites. Geochim. Cosmochim. Acta 63, 2623–2636.
Gainsforth, Z., et al., 2010. Coordinated TEM/STXM/IMS analysis of a type IIA chondrule fragment from comet 81P/Wild2 Stardust track C2052, 2, 74. Meteorit. Planet. Sci. 45 (Iss. Suppl. s1, A60, #5428).
Ganguly, J., Tazzoli, V., 1994. Fe^{2+}–Mg interdiffusion in orthopyroxene: retrieval from the data on intracrystalline reaction. Am. Mineral. 79, 930–937.
Genge, M., Gileski, A., Grady, M.M., 2005. Chondrules in Antarctic micrometeorites. Meteorit. Planet. Sci. 40, 225–238.
Gounelle, M., et al., 2005. Small Antarctic micrometeorites: A mineralogical and in situ oxygen isotope study. Meteorit. Planet. Sci. 40, 917–932.
Greenwood, J.P., Rubin, A.E., Wasson, J.T., 2000. Oxygen isotopes in R-chondrite magnetite and olivine: links between R chondrites and ordinary chondrites. Geochim. Cosmochim. Acta 64, 3897–3911.
Grossman, J.N., Brearley, A.J., 2005. The onset of metamorphism in ordinary and carbonaceous chondrites. Meteorit. Planet. Sci. 40, 87–122.
Haggerty, S.E., McMahon, B.M., 1979. Magnetite-sulfide-metal complexes in the Allende meteorite. Proc. 10th Lunar Planet. Sci. Conf, pp. 851–870.
Hörz, F., Zolensky, M.E., Bernhard, R.P., See, T.H., Warren, J.L., 2000. Impact features and projectile residues in aerogel exposed on Mir. Icarus 147, 559–579.
Hörz, F., et al., 2006. Impact features on stardust: implications for Comet 81P/Wild 2 Dust. Science 314, 1716–1719.
Jacob, D., Stodolna, J., Leroux, H., Langenhorst, F., Houdellier, F., 2009. Pyroxenes microstructure in comet 81P/Wild 2 terminal Stardust particles. Meteorit. Planet. Sci. 44, 1475–1488.
Jones, R.H., 1990. Petrology and mineralogy of type II, FeO-rich chondrules in Semarkona (LL3.0)—origin by closed-system fractional crystallization, with evidence for supercooling. Geochim. Cosmochim. Acta 54, 1785–1802.
Jones, R.H., 1992. On the relationship between isolated and chondrule olivine grains in the carbonaceous chondrites ALHA 77307. Geochim. Cosmochim. Acta 56, 467–482.
Jones, R.H., 1994. Petrology of FeO-poor, porphyritic pyroxene chondrules in the Semarkona chondrite. Geochim. Cosmochim. Acta 58, 5325–5340.
Jones, R.H., 1996. FeO-rich, porphyritic pyroxene chondrules in unequilibrated ordinary chondrites. Geochim. Cosmochim. Acta 60, 3115–3138.
Jones, R.H., Scott, E.R.D., 1989. Petrology and mineralogy of type IA chondrules in the Semarkona (LL 3.0) chondrite. Proc. 19th Lunar Planet. Sci. Conf, pp. 523–536.
Kimoto, Y., Yano, K., Ishizawa, J., Miyazaki, E., Yamagata, I., 2009. Passive space–environment-effect measurement on the international space station. J. Spacecraft Rockets 46, 22–27.
Kita, N.T., Kimura, M., Ushikubo, T., Valley, J.W., 2008. Oxygen isotope systematics of chondrules from the least equilibrated H chondrite. Lunar Planet. Sci. XXXIX (CD #2059).
Kita, N.T., Ushikubo, T., Fu, B., Valley, J.W., 2009. High precision SIMS oxygen isotope analyses and the effect of sample topography. Chem. Geol. 264, 43–57.
Kita, N.T., Nagahara, H., Tachibana, S., Tomomura, S., Spicuzza, M.J., Fournelle, J.H., Valley, J.W., 2010. High precision SIMS oxygen three isotope study of chondrules in LL3 chondrites: role of ambient gas during chondrule formation. Geochim. Cosmochim. Acta 74, 6610–6635.
Krot, A.N., Nagashima, K., Yoshitake, M., Yurimoto, H., 2010. Oxygen isotopic compositions of chondrules from the metal-rich chondrites Isheyevo (CH/CB_b), MAC 02675 (CB_b) and QUE 94627 (CB_b). Geochim. Cosmochim. Acta 74, 2190–2211.
Kuebler, K.E., Jolliff, B.L., Wang, A., Haskin, L.A., 2006. Extracting olivine (Fo–Fa) compositions from Raman spectral peak positions. Geochim. Cosmochim. Acta 70, 6201–6222.
Kunihiro, T., Rubin, A.E., Wasson, J.T., 2005. Oxygen-isotopic compositions of low-FeO relicts in high-FeO host chondrules in Acfer 094, a type 3.0 carbonaceous chondrite closely related to CM. Geochim. Cosmochim. Acta 69, 3831–3840.
Lauretta, D.S., Nagahara, H., Alexander, C.M.O.D., 2006. Petrology and origin of ferromagnesian silicate chondrules. In: Lauretta, D.S., McSween, H.Y. (Eds.), Meteorites and the Early Solar System II. The University of Arizona Press and Lunar and Planetary Institute, pp. 431–459.
Maurette, M., et al., 1991. A collection of diverse micrometeorites recovered from 100 tonnes of Antarctic blue ice. Nature 351, 44–47.
McKeegan, K.D., et al., 2006. Isotopic compositions of cometary matter returned by Stardust. Science 314, 1724–1728.
Nakamura, T., et al., 2008. Chondrulelike objects in short-period comet 81P/Wild 2. Science 321, 1664–1667.
Nakashima, D., et al., 2011. High precision oxygen three isotope analysis of Wild-2 particles and anhydrous chondritic interplantary dust particles. Lunar Planet. Sci. XXXXII (CD #1240).
Noguchi, T., Nakamura, T., Nozaki, W., 2002. Mineralogy of phyllosilicate-rich micrometeorites and comparison with Tagish Lake and Sayama meteorites. Earth Planet. Sci. Lett. 202, 229–246.
Raghavan, V., 2004. Fe–Ni–S (iron–nickel–sulfur). J. Phase Equilib. 25, 373–381.
Rubin, A.E., Wasson, J.T., 1988. Chondrules and matrix in the Ornans CO3 meteorites: possible precursor components. Geochim. Cosmochim. Acta 52, 425–532.
Sakamoto, N., et al., 2007. Remnants of the early solar system water enriched in heavy oxygen isotopes. Science 317, 231–233.
Schrader, D.L., Connolly Jr., H.C., Lauretta, D.S., 2008. Opaque phases in type-II chondrules from CR2 chondrites: implications for CR parent body formation. Geochim. Cosmochim. Acta 72, 6124–6140.
Schrader, D.L., Connolly Jr., H.C., Lauretta, D.S., 2010. On the nebular and aqueous signatures in the CR chondrites. Lunar Planet. Sci. XXXXI (CD #1262).
Seto, Y., et al., 2008. Mineralogical characterization of a unique material having heavy oxygen isotope anomaly in matrix of the primitive carbonaceous chondrite Acfer 094. Geochim. Cosmochim. Acta 72, 2723–2734.
Steagall, C., Smith, K., Soares, C., Mikatarian, R., Baba, N., 2009. Induced-contamination predictions for the micro-particle capturer and space environment exposure device. J. Spacecraft Rockets 46, 39–44.
Valley, J.W., Kita, N.T., 2009. In situ oxygen isotope geochemistry by ion microprobem. In: Fayek, M. (Ed.), Secondary Ion Mass Spectrometry in the Earth Sciences. Mineralogical Association of Canada Short Course, 41. Mineralogical Association of Canada, Québec, pp. 19–63.
Weisberg, M.K., Prinz, M., 1994. Agglomeratic olivine (AO) chondrules in ordinary chondrites. Lunar Planet. Sci. XXV, 1481–1482.
Weisberg, M.K., Ebel, D.S., Kimura, M., Kita, N.T., Nakashima, D., 2010. Petrology and oxygen isotopes of chondrules in the Kota Kota EH3 chondrite. Lunar Planet. Sci. XXXXI (CD #1756).
Yurimoto, H., et al., 2008. Oxygen isotopes of chondritic components. In: MacPherson, G.J., et al. (Ed.), *Oxygen in the Solar System*, *Reviews in Mineralogy and Geochemistry*, 68. Mineralogical Society of America, pp. 141–186.
Zolensky, M.E., et al., 2006. Mineralogy and petrology of comet 81P/Wild 2 nucleus samples. Science 314, 1735–1739.